



Structural and electronic trends of optical cycling centers in polyatomic molecules revealed by microwave spectroscopy of MgCCH, CaCCH, and SrCCH

P. Bryan Changala^{a,1} , Nadav Genossar-Dan^b , Ella Brudner^b, Tomer Gur^b , Joshua H. Baraban^b , and Michael C. McCarthy^a

Edited by Anna I. Krylov, University of Southern California, Los Angeles, CA; received March 3, 2023; accepted May 23, 2023 by Editorial Board Member Shaul Mukamel

The unique optical cycling efficiency of alkaline earth metal-ligand molecules has enabled significant advances in polyatomic laser cooling and trapping. Rotational spectroscopy is an ideal tool for probing the molecular properties that underpin optical cycling, thereby elucidating the design principles for expanding the chemical diversity and scope of these platforms for quantum science. We present a comprehensive study of the structure and electronic properties in alkaline earth metal acetylides with highresolution microwave spectra of 17 isotopologues of MgCCH, CaCCH, and SrCCH in their ${}^2\Sigma^+$ ground electronic states. The precise semiexperimental equilibrium geometry of each species has been derived by correcting the measured rotational constants for electronic and zero-point vibrational contributions calculated with highlevel quantum chemistry methods. The well-resolved hyperfine structure associated with the ^{1,2}H, ¹³C, and metal nuclear spins provides further information on the distribution and hybridization of the metal-centered, optically active unpaired electron. Together, these measurements allow us to correlate trends in chemical bonding and structure with the electronic properties that promote efficient optical cycling essential to next-generation experiments in precision measurement and quantum control of complex polyatomic molecules.

optical cycling | electronic properties | molecular spectroscopy

Direct laser cooling of molecules has become an essential tool in a broad array of applications spanning ultracold chemistry, precision metrology, and quantum simulation and information (1, 2). Since the first demonstrations of laser slowing, cooling, and trapping with diatomics (3–14), the chemical complexity of molecular targets has steadily grown, with recent examples of both linear (15-18) and nonlinear (19-21) polyatomic molecules. Maintaining both high laser-cooling performance and suitability for the application of interest has motivated new ways of engineering functional versatility, including hypermetallic molecules (22-24) and chemically tuned substituents (25, 26). Understanding the basic connections between laser-cooling efficiency and molecular structure thus provides vital insights toward formulating general design principles in this increasingly expanding and diverse chemical space (27).

One of the most common paradigms for laser-coolable molecules is an alkaline earth (or alkaline earth-like) metal, M, with an s² valence configuration bonded to a monovalent, electronegative ligand, L, such as F, OH, or CCH. The electronic configuration of these systems is best described as M⁺L⁻, with one metal s electron donated to the ligand and the remaining unpaired electron occupying a hybridized metal-centered $\sigma(sp)$ orbital highly polarized away from the ligand (28). The unpaired electron interacts only weakly with the rest of the molecule, and its electronic excitations lead to remarkably small changes in molecular geometry and vibrational frequencies, resulting in highly diagonal Franck-Condon factors (FCFs) (21, 29-32) enabling optical cycling of thousands of photons and therefore successful cooling while avoiding transfer of electronic energy to the vibrational degrees of freedom. The viability of this approach has been borne out by a plethora of examples, differing in both the metal atom, e.g., Ca (11, 19, 29), Sr (5, 16), and Yb (12, 15, 21, 32) and ligand, e.g., F (5, 11, 12), OH (15, 16, 29, 32), and OCH₃ (19, 21). The relative insensitivity to the details of the ligand's structure has made this M-L template a promising concept to extend to large polyatomic systems, such as functionalized aromatic hydrocarbons (27) and

Metal-ligand molecules containing the ethynyl or acetylide group, -CC-, offer the possibility of accommodating multiple metal centers, i.e., MCCM' (22, 23, 33), whose

Significance

Laser-cooled molecules have enabled ground-breaking advances in quantum science. Transferring sophisticated optical cycling-based cooling techniques developed for simple diatomic molecules to complex polyatomic molecules remains a challenge, but will enable experiments of greater sensitivity and versatility. Achieving this goal requires a comprehensive understanding of the chemical properties that influence optical cycling efficiency. Using microwave rotational spectroscopy, we have derived precise structures and electronic properties for a family of metal-ligand radicals. We identify subtle but significant changes in bond lengths, electron distribution, and orbital hybridization to be quantitative measures of the ionic metalligand bonding character critical to efficient optical cycling. This work provides a foundation for elucidating transferable design principles for assessing how chemical modifications affect laser-cooling performance in larger molecules.

The authors declare no competing interest.

This article is a PNAS Direct Submission. A.I.K. is a guest editor invited by the Editorial Board.

Copyright © 2023 the Author(s). Published by PNAS. This article is distributed under Creative Commons Attribution-NonCommercial-NoDerivatives License 4.0 (CC BY-NC-ND).

¹To whom correspondence may be addressed. Email: bryan.changala@cfa.harvard.edu.

This article contains supporting information online at https://www.pnas.org/lookup/suppl/doi:10.1073/pnas. 2303586120/-/DCSupplemental.

Published July 3, 2023.

interactions can be tuned simply by elongation with repeated C_2 units, i.e., $M(CC)_nM'$. Characterizing the chemical structure and electronic properties of these hypermetallic molecules first requires a detailed understanding of the parent monometallic acetylides, MCCH. We focus here on the three alkaline earth metal-containing species MgCCH, CaCCH, and SrCCH. Although the rotational and electronic spectra of these systems have been investigated in a number of previous millimeterwave (34–37) and optical (38–54) studies, our knowledge of their precise ground-state structures and electronic parameters is incomplete.

A comprehensive description of these molecular properties is crucial to understanding the influence of chemical modifications and substitutions on optical cycling in metal-bearing carbon chains. In this paper, we establish a reference standard with a cavity Fourier transform microwave (FTMW) study of 17 isotopologues of MgCCH, CaCCH, and SrCCH. The rotational constants, combined with ab initio corrections for zero-point and electronic effects, allow precise semiexperimental equilibrium structures to be derived. The well-resolved ^{1,2}H, ¹³C, ²⁵Mg, and ⁸⁷Sr magnetic hyperfine structure has also been analyzed, providing detailed information on the ground-state electronic structure for these three systems, in particular the distribution of the unpaired electron used for optical cycling. By examining trends in structure, bonding, and hybridization down Group IIA of the Periodic Table, we show that the CCH ligand in the three examined cases is largely insensitive to the identity of the metal, as shown by both the equilibrium geometries and by the unpaired electron distribution, which is highly localized around the metal. These properties confirm the high suitability of metal acetylides for optical cycling applications and support the possible extension to their bimetallic analogues. Finally, a comparison between our measurements and high-accuracy coupled cluster calculations provides a robust benchmark for applying these quantum chemical methods to structural and electronic property calculations of this family of molecules. These results pave the way toward future experimental and theoretical studies of larger, chemically functionalized, or multiple metal-bearing acetylides en route to novel laser cooling applications.

Results

Rotationally cold MCCH molecules were produced in the gas phase via a laser-ablation supersonic expansion source and probed with a cavity microwave spectrometer in the 5- to 26-GHz frequency range. Seventeen isotopologues were detected in total. Such a large dataset is necessary to derive complete chemical structures and unpaired electron spin distributions. Isotopes with nonzero nuclear spin were observed for all elements with the exception of calcium due to the low natural abundance of the ⁴³Ca isotope (0.14%). Further experimental details are described in *Materials and Methods*.

The MCCH species each have a ${}^2\Sigma^+$ ground electronic state with a relatively simple fine and hyperfine structure. In addition to a spin-rotation interaction, $\gamma \mathbf{N} \cdot \mathbf{S}$, each nucleus with I > 0 has an isotropic Fermi contact term, $b_F \mathbf{I} \cdot \mathbf{S}$, and an anisotropic spin-spin interaction, $c(I_z S_z - \mathbf{I} \cdot \mathbf{S}/3)$ (55). The D, ${}^{25}\mathrm{Mg}$, and ${}^{87}\mathrm{Sr}$ nuclei all have $I \geq 1$ and thus experience additional electric quadrupole interactions with the molecular electric field gradient characterized by the usual eQq constant (56). The rotation (B), centrifugal distortion (D), spin-rotation (γ), and hyperfine (b_F , c, eQq) parameters were least-squares optimized to the measured transition frequencies with the SPFIT program (57). The experimental line lists and fit files are available in SI Appendix. The best-fit spectroscopic constants are summarized in Tables 1–3.

Semiexperimental equilibrium structures (r_{se}) were derived by adjusting the three bond lengths to reproduce the measured B values. For a given isotopologue, the ground-state B_0 value was calculated as

$$B_0 = B_e \left(1 + g \frac{m_e}{m_p} \right) - \Delta_{\text{vib}},$$
 [1]

where B_e is the rotational constant evaluated at the equilibrium geometry with atomic masses (60), g is the electronic g-tensor correction, $m_e/m_p \approx 1/1836.153$ is the electron-to-proton mass ratio, and $\Delta_{\rm vib} = B_e - B_0$ is the calculated vibrational zero-point correction (reported for each isotopologue in Tables 1–3). The best-fit bond lengths are presented in Table 4.

Table 1. Spectroscopic constants of MgCCH

Parameter*	²⁴ MgCCH	²⁴ MgCCD	²⁴ Mg ¹³ CCH	²⁴ MgC ¹³ CH	²⁶ MgCCH	²⁵ MgCCH
В	4965.3354(2)	4584.1538(3)	4944.2159(15)	4803.0410(9)	4792.1641(2)	4875.3068(3)
$D \times 10^3$	$[2.2324]^{\dagger}$	[2.2324] [†]	[2.2324] [†]	[2.2324] [†]	[2.2324] [†]	[2.2324] [†]
γ	16.659(1)	15.374(1)	16.987(12)	15.794(11)	16.080(1)	16.358(2)
$b_F(H/D)$	4.7177(17)	0.6782(29)	[4.7177] [‡]	[4.7177] [‡]	4.7159(20)	4.752(48)
c(H/D)	1.842(4)	0.306(6)	[1.842] [‡]	[1.842] [‡]	1.840(5)	1.845(43)
eQq(D)		0.165(7)				
b_F (C/Mg)			163.0(8)	17.96(2)		-273.8(10)
c(C/Mg)			17.07(8)	2.34(13)		-15.178(7)
eQq(Mg)						-35.06(2)
RMS error ×10 ³	0.6	9.1	27	8.1	7.0	6.1
$B_e - B_0^{\S}$	-14.8038	-14.9241	-13.6718	-14.5574	-14.3499	-14.5680
g^{\P} (dimensionless)	-0.0252	-0.0229	-0.0250	-0.0241	-0.0247	-0.0249

 $^{^*}$ All values are given in MHz. The estimated 1 σ uncertainties are given in parentheses in units of the last decimal place.

 $^{^{\}dagger}$ D was fixed to the measured mm-wave value of the main isotopologue (35).

[‡]Hydrogen hyperfine parameters were fixed to the values of the main isotopologue.

 $[\]S$ Calculated at the VPT2/AE-CCSD(T)/cc-pCVTZ level of theory.

The g-tensor for the main isotopologue was calculated at the FC-CCSD(T)/cc-pVQZ level of theory. The values for the other isotopologues were determined by the isotope shift relations for linear molecules (58) assuming an electric dipole moment of 1.68 D (59).

Table 2. Spectroscopic constants of CaCCH

Parameter*	⁴⁰ CaCCH	⁴⁰ CaCCD	⁴⁰ Ca ¹³ CCH	⁴⁰ CaC ¹³ CH	⁴⁴ CaCCH
В	3396.4910(3)	3148.2686(4)	3365.6507(3)	3273.3888(4)	3286.8162(6)
$D \times 10^3$	1.28(3)	1.15(2)	1.26(2)	1.27(3)	1.16(6)
γ	21.941(7)	20.351(1)	21.752(1)	21.167(3)	21.233(2)
$b_F(H/D)$	2.097(2)	0.318(1)	[2.097] [†]	[2.097] [†]	[2.097] [†]
c(H/D)	1.235(4)	0.193(3)	[1.235] [†]	[1.235] [†]	[1.235] [†]
eQq(D)		0.197(3)			
$b_F(C)$			67.194(10)	4.479(45)	
c(C)			6.076(5)	2.465(48)	
RMS error ×10 ³	1.2	3.2	1.2	6.0	1.2
$B_e-{B_0}^{\ddagger}$	-16.4036	-15.6702	-15.3170	-15.9770	-15.9296
g§ (dimensionless)	-0.0338	-0.0306	-0.0333	-0.0321	-0.0337

^{*}All values are given in MHz. The estimated 1σ uncertainties are given in parentheses in units of the last decimal place.

The $r_{\rm se}$ structure of C₂H⁻, an important benchmark for comparison to the MCCH molecules, does not appear to have been reported in the literature, but most of the required data are available, including the experimental rotational constants for the normal and singly substituted ¹³C species (61). Using the high-quality zero-point corrections calculated by Huang and Lee (62) (from their best "+AC/AVTQ5Z" quartic force field), as well as our calculated g value of -0.1789 (FC-CCSD(T)/cc-pVQZ) and a permanent dipole moment of 3.093 D (63), we fitted the $r_{\rm se}$ structure in the same manner as for the metal acetylides. The optimized bond lengths are included in Table 4.

The theoretical results for the high-accuracy ab initio geometries, equilibrium and vibrationally averaged dipole moments, centrifugal distortion parameters, and (hyper)fine spectroscopic constants are summarized in Table 5 (see *Materials and Methods* for further details). The reported values are for the main isotopologues, i.e., the most abundant isotopic species. The

various contributions to our best-estimate theoretical geometries and results for other isotopologues are given in *SI Appendix*, Tables S1–S3.

The magnetic hyperfine parameters are more easily compared between two nuclei when converted to their nucleus-independent, intrinsic electronic factors. The unpaired electronic spin density at a given nucleus, ρ_0 , can be determined from the measured b_F values by the relation

$$b_F = 800.2374 \text{ MHz} \times g_I \rho_0,$$
 [2]

where g_I is the nuclear g-factor (55). The spin anisotropy about each nucleus is determined from the hyperfine constant c through the relation

$$c = 143.281956 \text{ MHz} \times g_I \left(\frac{3\cos^2 \theta - 1}{r^3} \right)_{\text{unpaired}},$$
 [3]

Table 3. Spectroscopic constants of SrCCH

Parameter*	⁸⁸ SrCCH	⁸⁸ SrCCD	⁸⁸ Sr ¹³ CCH	⁸⁸ SrC ¹³ CH	⁸⁶ SrCCH	⁸⁷ SrCCH
В	2499.6121(3)	2313.2700(2)	2461.4657(2)	2395.0867(2)	2511.7261(3)	2505.5933(1)
$D \times 10^3$	0.802(10)	0.662(6)	0.788(8)	0.748(8)	0.801(11)	[0.802] [†]
γ	51.228(1)	47.443(2)	50.467(1)	49.086(1)	51.475(2)	51.290(2)
$b_F(H/D)$	1.877(7)	0.292(13)	[1.877] [‡]	[1.877] [‡]	1.865(30)	[1.877] [‡]
c(H/D)	1.129(9)	0.186(13)	[1.129] [‡]	[1.129] [‡]	1.202(15)	[1.129] [‡]
eQq(D)		0.199(20)				
$b_F(C/Sr)$			59.386(7)	3.641(13)		-525.7(2)
<i>c</i> (C/Sr)			5.283(14)	1.864(17)		-27.987(8)
eQq(Sr)						-144.86(4)
RMS error ×10 ³	0.6	3.0	1.3	2.7	1.2	16.7
$B_e - B_0^{\S}$	-11.6679	-11.3308	-10.7511	-11.3594	-11.7190	-11.6931
g^{\P} (dimensionless)	-0.0907	-0.0834	-0.0891	-0.0865	-0.0909	-0.0908

^{*}All values are given in MHz. The estimated 1σ uncertainties are given in parentheses in units of the last decimal place.

[†] Hydrogen hyperfine parameters were fixed to the values of the main isotopologue.

[‡]Calculated at the VPT2/AE-CCSD(T)/cc-pCVTZ level of theory using the ECP10MDF pseudopotential and cc-pCVTZ-PP basis set for Ca.

[§]The g-tensor for the main isotopologue was calculated at the FC-CCSD(T)/cc-pVQZ level of theory. The values for the other isotopologues were determined (58) assuming an electric dipole moment of 2.744 D (calculated in this work).

 $^{^{\}dagger}$ D was fixed to the value of the main isotopologue.

[‡]Hydrogen hyperfine parameters were fixed to the values of the main isotopologue.

[§] Calculated at the VPT2/AE-CCSD(T)/cc-pCVTZ level of theory using the ECP28MDF pseudopotential and cc-pCVTZ-PP basis set for Sr.

The g-tensor for the main isotopologue was calculated at the FC-CCSD(T)/cc-pVQZ level of theory. The values for the other isotopologues were determined (58) assuming an electric dipole moment of 3.622 D (calculated in this work).

Table 4. Semiexperimental equilibrium geometries of MCCH and related species

Parameter*	MgCCH [†]	CaCCH [†]	SrCCH [†]
r _{MC} r _{CC} r _{CH} RMS error [‡]	2.0369(7) 1.2247(9) 1.0647(5) 0.031	2.3106(4) 1.2282(6) 1.0655(4) 0.010	2.4531(25) 1.2279(40) 1.0695(25) 0.051
r _{CC} r _{CH} RMS error [‡]	HCCH [§] 1.20282(1) 1.06169(2)	CCH [¶] 1.207(2) 1.069(2)	CCH ^{-†} 1.2460(3) 1.0698(13) 0.129

^{*}All bond lengths are given in Å. The estimated 2σ uncertainties are shown in parentheses. † r_{se} determined in this work. See text for details.

where the last factor on the right-hand side is the spin anisotropy, with r the distance of the unpaired electron from the given nucleus, and θ the angle of this vector with the molecular axis. $\langle \cdots \rangle_{\text{unpaired}}$ is the expectation value over the unpaired electron spin density in atomic units. The derived values of ρ_0 and $\langle \cdots \rangle_{\text{unpaired}}$ are shown in Fig. 1.

Discussion

Equilibrium Geometries. The structural and electronic properties of the MCCH molecules can be interpreted as arising from an $M^+[CCH]^-$ electronic configuration, i.e., an effectively closed-shell CCH⁻ ligand ionically bonded to a metal cation, with the unpaired electron occupying a nonbonding metal-centered $\sigma(sp)$ orbital (28). This picture is illustrated by the derived r_{se} structures (Table 4). There is a monotonic increase in the metal-carbon bond length with heavier metals due to the progressively larger metal atomic radius, while bond lengths of the CCH ligand itself are remarkably insensitive to the identity of the metal. Other series of monovalent ligands show structural patterns comparable to the acetylides. Both the metal fluorides, MgF [$r_e = 1.7499 \text{ Å}(68)$], CaF [$r_e = 1.9516 \text{ Å}(69)$], and SrF [$r_e = 2.0753 \text{ Å}(70)$], and hydroxides, MgOH [$r_{MgO} \approx 1.767 \text{ Å}(71)$], CaOH [$r_{CaO} = 1.9751 \text{ Å}(72)$], and SrOH

Table 5. Theoretical values for the geometries and spectroscopic constants of the MCCH molecules

Parameter*	MgCCH	CaCCH	SrCCH
r_{MC}	2.03884	2.31229	2.45857
$r_{\rm CC}$	1.22638	1.23015	1.23094
r_{CH}	1.06476	1.06539	1.06557
μе	1.64	2.71	3.47
μ_0	1.75	2.81	3.58
$D \times 10^3$	1.94	1.05	0.60
γ^{\dagger}	17.8		
$eQq(^{25}Mg/^{43}Ca)$	-34.6	-14.3	
eQq(D)	0.22	0.22	0.22

^{*}Bond lengths are given in Å, equilibrium (μ_e) and vibrationally averaged (μ_0) dipole moments in Debye, and all other constants in MHz.

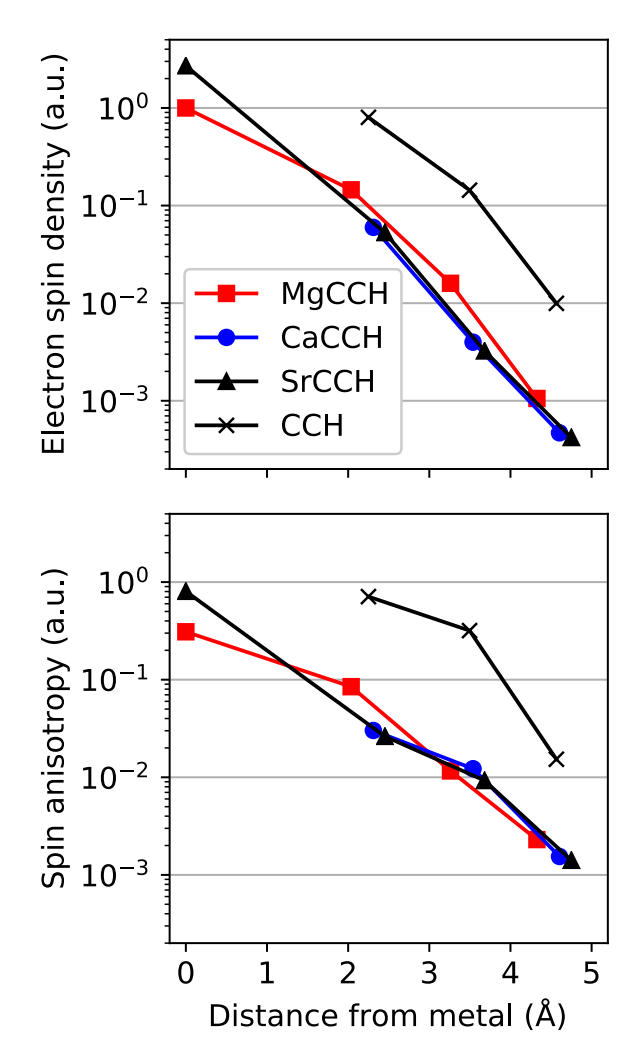


Fig. 1. Unpaired electron distribution in MCCH molecules. The *Top* panel shows the spin density at each nucleus versus its distance from the metal atom (Eq. **2**). The *Bottom* panel shows the spin anisotropy with respect to each nucleus (Eq. **3**). The values for CCH (66, 67) are plotted with a fictitious M-C distance of 2.25 Å for ease of comparison.

[r_{SrO} ≈ 2.11 Å (73)], have a similar metal-dependence, but their metal-ligand bonds are about 0.3 to 0.4 Å shorter as a whole than those in the respective acetylides. Our measured metal-carbon bond lengths differ by up to 40 mÅ from the estimates derived from earlier mm-wave studies (35–37), wherein only measurements of the main MCCH isotopologues were available, which in turn required the CCH bond lengths to be constrained to those of HCCH. Our complete isotopic dataset shows, however, that this is generally not a good enough approximation at mÅ precision. For example, the C≡C bond length in each of the three MCCH molecules studied here is about 20 mÅ longer than in neutral HCCH or CCH radical. This is about half the difference between either of the neutral species and CCH[−] anion, showing that a significant fraction of an electron is transferred to the CCH ligand.

A comparison of the theoretical structures (Table 5) with the r_{se} bond lengths is very favorable. The calculated errors are the same order of magnitude as the r_{se} uncertainties and not more than 5 mÅ for any bond. It is worth mentioning the relatively large contributions of the high-level correlation correction to the theoretical geometries (*SI Appendix*, Table S1), which were on the order of a few mÅ for the C \equiv C bonds.

 $^{^{\}ddagger}$ RMS error of the fitted B_0 constants in MHz.

[§] Ref. 64

[¶] Ref. 65.

 $^{^\}dagger$ Calculations of the spin-rotation coupling constants for Ca and Sr are currently unavailable for effective core potentials.

The importance of including high-level correlation effects in systems that involve interactions between multiple electron pairs, such as triple bonds, conjugated π systems or adjacent lone pairs, has been reported in previous studies (74–77). Although the accurate structural predictions suggest that the underlying potential energy surfaces are reliable, we note that the calculated centrifugal distortion constants are all too low by 10 to 25%. We did find good agreement between the calculated VPT2 anharmonic vibrational frequencies and vibration-rotation constants with existing literature data (*SI Appendix*, Tables S4 and S5), suggesting that this discrepancy might be due to effects associated with higher-order centrifugal distortion.

Electronic Properties. The best-fit hyperfine constants provide a fairly direct characterization of the ground-state electronic wavefunction. The spin densities derived from the b_F parameters, shown in Fig. 1, vividly illustrate the confinement of the unpaired electron to the metal atom. The spin density along the molecular axis decays approximately exponentially with the distance from the metal nucleus, decreasing by an order of magnitude every \sim 1.1 Å. The spin anisotropy exhibits a similar pattern, but with an attenuated rate of an order of magnitude only every ~ 1.6 Å, such that the anisotropy relative to the local spin density is actually increasing. Judging from the relative spin densities of the metal vs. ligand, the localization in CaCCH and SrCCH is more pronounced than in MgCCH, reflective of less ionic character for Mg. These small but significant differences aside, the MCCH spin distributions are remarkably consistent. Each shows a pronounced decrease in the total spin population on the CCH ligand compared to the free CCH radical, the spin densities and anisotropies of which are a factor of 10 to 40 larger (66, 67). The calculated spin densities and anisotropies (SI Appendix, Table S2) reproduce these patterns, although their fractional accuracy degrades for nuclei with the smallest spin populations. The parameters for Mg (the only metal nucleus for which both experimental and theoretical data are available) are computed to within a few percent error, the neighboring ¹³C atom to within 25%, and the next ¹³C atom to within a factor of about two. The calculated H/D spin anisotropies are also within a factor of two of the measured values, but the corresponding spin densities are only accurate to an order of magnitude and of indeterminant sign, reflecting the sensitivity of multiple small contributions (including vibrational averaging effects neglected here) to nuclei far from localized spin centers.

The orbital hybridization of the unpaired electron can be inferred from the spin density and anisotropy measured at the metal nucleus. Comparing the spin densities to their values in the ${}^2S_{1/2}$ ground state of the corresponding atomic M⁺ cations gives some indication of s_{σ} , the σ orbital's fractional s character. For MgCCH, this ratio is 0.46 (78, 79) and for SrCCH, 0.53 (80). A similar comparison between the metal-centered spin anisotropy and that of the ${}^{2}P_{3/2}$ M⁺ excited state indicates the complementary p character, which is $p_{\sigma} \approx 0.32$ and 0.33 for Mg and Sr, respectively (81–83). That the estimated s_{σ} and p_{σ} fractions do not sum to unity probably reflects the different $\langle r^{-3} \rangle$ radial extent of the molecular and cation orbitals. For example, using the spin parameters for the excited 3s3p (^{3}P) manifold of neutral Mg (84) instead, the estimated s_{σ} and p_{σ} character in MgCCH both increase to 0.58 and 0.45, respectively. The corresponding values using neutral Sr atomic parameters (85) for SrCCH are $s_{\sigma}=0.67$ and $p_{\sigma}=0.42$. In both neutral cases, s_{σ} and p_{σ} now sum to slightly greater than unity. The molecular σ orbitals therefore appear to be built from atomic

orbitals intermediate between the bare atomic cation and neutral orbitals. Despite these uncertainties, the ratio of the s_{σ} and p_{σ} character (about 1.3 to 1.6:1) is similar using either reference and indicates that the metal-centered σ orbitals in MgCCH and SrCCH are both hybridized with extensive p character directing the σ lobe away from the CCH ligand.

This p_{σ} character induces a large contribution to the spin-rotation constant in the $^{2}\Sigma^{+}$ ground state via second-order spin-orbit coupling with nearby $^{2}\Pi$ states. Because the unpaired spin is localized in metal-centered orbitals, this contribution is approximately

$$\gamma \approx 4B\zeta p_{\sigma}p_{\pi}/E_{\Pi-\Sigma},$$
 [4]

where B is the rotational constant, ζ is the metal's effective atomic spin-orbit coupling constant, $E_{\Pi-\Sigma}$ is the vertical excitation energy of the lowest ${}^2\Pi$ state, and p_{σ} and p_{π} are the p characters of the singly occupied $\sigma(sp)$ and $\pi(pd)$ orbitals in the $^2\Sigma^+$ and ${}^2\Pi$ states, respectively. The atomic ζ values for the valence p orbitals are 41 and 61 cm⁻¹ for Mg and Mg⁺; 87 and 149 cm⁻¹ for Ca and Ca⁺; and 387 and 534 cm⁻¹ for Sr and Sr^+ . Using the $E_{\Pi-\Sigma}$ vertical energies from Ivanov et al. (23), and approximating $p_{\sigma}p_{\pi}\approx 0.5\times 0.5=0.25$, the spinorbit contribution to γ is about 9 to 13 MHz for MgCCH, 19 to 32 MHz for CaCCH, and 67 to 92 MHz for SrCCH, where the range indicates the values using the neutral and cation atomic ζ values. These crude estimates are within a factor of two of the experimentally derived values, 16.7 MHz, 21.9 MHz, and 51.2 MHz, respectively, which suggests that spin-orbit interactions are indeed the dominant contributor to the spinrotation parameters. [It is also worth noting that the Mulliken spin populations for the ground electronic state indicate p_{σ} may be as low as 0.2 to 0.3, but in this case, the p_{π} character of the excited orbital likely is correspondingly higher, such that $p_{\sigma}p_{\pi}$ is qualitatively insensitive to such changes. The ab initio result for MgCCH (Table 5) is, in any case, in good agreement with the measured γ value.]

High-resolution optical spectroscopy of the excited $\tilde{A}^2\Pi$ state of each MCCH molecule provides an additional constraint to this analysis. The first-order spin—orbit constant of this state is approximately $A_{\Pi} = \zeta p_{\pi}$, the product of the effective atomic ζ value and the p character of the excited π orbital (ignoring the much smaller contribution from d orbitals). Using the measured values (44, 51, 54) $A_{\Pi}(MgCCH) = 36.146 \text{ cm}^{-1}$, $A_{\Pi}(CaCCH) = 70.822 \text{ cm}^{-1}$, and $A_{\Pi}(SrCCH) = 272.180 \text{ cm}^{-1}$, the inferred ground-state p_{σ} character via Eq. 4 is 0.54, 0.36, and 0.27 for MgCCH, CaCCH, and SrCCH, respectively. From a comparison of these p_{σ} values to those from the spin anisotropy analysis above, it appears that the Mg molecular orbitals are more similar to its neutral atomic orbitals, while the Sr molecular orbitals are more similar to its cation atomic orbitals, consistent with the general increase in ionic bonding character down Group IIA.

The nuclear quadrupole coupling constants provide information on the total electron distribution via the electric field gradient of both the unpaired and paired electron populations, complementary to the magnetic fine and hyperfine structure, which is sensitive only to the unpaired electron. The contribution to eQq of a given nucleus from the unpaired spin density is directly proportional to the spin anisotropy at the same nucleus $(eQq = -1.63988 \times (Q/barns) c/g)$ (56). Inspection of the deuterium eQq and c parameters shows that the unpaired spin contribution to the former is negligible (1% or less),

and therefore eQq is determined entirely by the local C-D covalent bonding environment. The measured MCCD eQq values (ca. 170 to 200 kHz) are similar to other C-D single bonds, e.g., 194(2) kHz for DCN (86), 191.5(8) kHz for CH₃D (87), and 209(1) kHz for DCCD (88). In contrast, the metal eQq parameters have a significant contribution from the unpaired electron—approximately 40% for both ²⁵MgCCH and 87 SrCCH. The remaining 60% (i.e., -20.6 MHz for 25 MgCCH and -87.3 MHz for 87 SrCCH) is due to charge polarization of the closed-shell core. After correcting for differences in their nuclear quadrupole moments, the core-polarized field gradient in SrCCH is nearly 3× greater than in MgCCH, despite the longer metal-carbon bond length (which thereby decreases the electric field-induced polarization due to the CCH- anion). The increase is presumably due simply to the larger polarizability of the Sr^{2+} core itself, the free-ion value of which is about $10\times$ larger than Mg²⁺ (89). It is also interesting to compare the corepolarization contribution of ²⁵MgCCH to the eQq constant of NaCCH (90) (which is due entirely to core polarization). After scaling for the ratio of the nuclear quadrupole moments, the electric field gradient in NaCCH is about 32% smaller than the core-polarization contribution in MgCCH, despite the free Na⁺ ion having a polarizability $2 \times \text{ larger than } \text{Mg}^{2+}$ (91).

Implications for Optical Cycling and Quantum Control. The $\tilde{A}^2\Pi - \tilde{X}^2\Sigma^+$ electronic transition—the primary candidate for optical cycling in MCCH molecules—has been studied in MgCCH (38, 39, 51), CaCCH (40–46, 53), and SrCCH (40, 50, 54) by medium- to high-resolution laser spectroscopy. Although their fluorescence vibrational branching ratios have not yet been measured as comprehensively and quantitatively as the related hydroxides (31, 32), it is clear from these studies that the FCFs in CaCCH and SrCCH are more diagonal than in MgCCH. The $\Delta v = 1$ vibronic transitions of the v_3 M–C stretching mode, for example, have comparable oscillator strength to the v = 0 - 0origin transition in MgCCH (39, 51), but are one to two orders of magnitude weaker in CaCCH (46) and SrCCH (50).

The established ionic M⁺L⁻ bonding picture provides a framework to assess these manifest differences in optical properties and to connect them to the ground-state electronic structure. The most directly relevant trend we observe is the unpaired electron distributions in MgCCH vs. CaCCH and SrCCH (Fig. 1). These distributions demonstrate that although each MCCH molecule is highly ionic, there are subtle but significant variations in their electronic structure. The spin density on the CCH ligand is a factor of 2 to 4× smaller in the heavier species compared to MgCCH. This grouping of Mg vs. Ca and Sr is in turn correlated with their similarly distributed electropositivities [ionization potentials of 7.6 vs. 6.1 and 5.7 eV, respectively (92)] and the polarizability of their valence s/p orbitals [$\alpha = 71$ vs. 161 and 197 a.u., respectively (93)], which together promote radical localization away from the ligand in the heavier metals. These trends are reinforced by differences in the excited molecular orbitals: the Mg $\pi(3pd)$ orbital has a greater overlap with the C \equiv C π system relative to the larger Ca $\pi(4pd)$ and Sr $\pi(5pd)$ orbitals, contributing to a larger change in geometry upon $\pi \leftarrow \sigma$ excitation and thus less diagonal FCFs.

Nonradiative loss channels are an additional complication in MCCH molecules that can drastically reduce their optical cycling efficiency. Comparative absorption and fluorescence detection studies of the $\tilde{B}^2\Pi - \tilde{X}^2\Sigma^+$ ($\sigma(4pd) \leftarrow \sigma(4sp)$) transition in CaCCH (52, 53), for example, show an undetectably small

fluorescence quantum yield for this excited state, suggesting loss through some as of yet unidentified pathway. The electronic energy (ca. 16,500 cm⁻¹) is insufficiently high to predissociate via Ca + C₂H or CaC₂ + H, which have bond dissociation energies approximately twice as large (94, 95). Rapid internal conversion to highly vibrationally excited levels of the \tilde{X} state or multiphoton ionization/dissociation remain speculative possibilities. While the \tilde{A} state does not appear to be strongly affected by this mechanism, we stress that even a small branching ratio of, say, 1% would represent an important loss channel. Because these loss pathways direct population to a continuum (predissociation) or dense quasi-continuum (internal conversion), they cannot be experimentally recovered by optical repumping schemes. The same M⁺L⁻ electronic structure that promotes highly diagonal FCFs by isolating the metal-centered electronic structure from the polyatomic ligand will also suppress losses via these intramolecular processes.

Another important factor that controls internal conversion and vibrational energy redistribution is the vibrational density of states at an internal energy equal to the electronic excitation, which is strongly dependent on the ground-state vibrational frequencies. Using our calculated anharmonic fundamental frequencies (SI Appendix, Table S4), the density of vibrationally excited \tilde{X} state levels at the $\tilde{A}-\tilde{X}$ transition energy is approximately $\rho = 5{,}000/\text{cm}^{-1}$ for both CaCCH and SrCCH. This high state density is driven primarily by low-frequency stretching and bending modes involving the heavy metal atom. The lifetime due to leakage into this quasi-continuum can be estimated using Fermi's golden rule (96), $\tau \approx h/\rho \langle V^2 \rangle$, which indicates that an average coupling strength as small as $\sqrt{\langle V^2 \rangle} \sim 10^{-4}~{
m cm}^{-1}$ could compete nonnegligibly with the radiative lifetime, $au_{
m rad} \approx 25~{
m ns}$ (94). Accurate measurements and theoretical studies of the MCCH electronic transitions including their fluorescence (30), dissociative, and other nonradiative loss mechanisms will further refine the connections between optical cycling efficiency and ground-state electronic properties.

While the focus of our discussion has been on the application of hyperfine-resolved spectroscopy to elucidate electronic features relevant to optical cycling properties, the precisely determined spectroscopic constants themselves are also critical input to quantum control schemes for odd isotopologues. The complex level structure associated with such systems has been highlighted by recent studies of ^{171,173}YbOH (97) and ¹³⁷Ba¹⁹F (98), the heavy-nucleus spins of which probe a variety of new physics (1). An obvious extension of the MCCH studies reported in this paper is to isovalent YbCCH, a preliminary microwave isotopic analysis of which in our laboratory is already complete. A comparison of its electronic structure to both YbOH and the alkaline earth metal MCCH molecules will advance applications of these important heavy species.

Light-isotope spins, i.e., H and ¹³C, are less relevant to new physics searches, but they represent a potentially useful quantum resource in polyatomic molecules (99). The five proton spins in the laser-cooling candidate calcium phenoxide, CaOC₆H₅ (20), for example, provide a relatively large and readily manipulated spin-rotation state space. Although the complexity of the fine-hyperfine structure of such many-spin radicals grows exponentially with the number of spins, cavity microwave studies of organic ligands with the same number of protons, e.g., phenyl radical, c-C₆H₅ (100) suggest that a comprehensive and exhaustive understanding of the hyperfine structure of the corresponding metal-ligand molecule is attainable by similar means.

Conclusion

We have presented a comprehensive analysis of the precise ground-state molecular and electronic structure of the alkaline earth metal acetylides. These results lay a foundation for understanding how and why ionicity, hybridization, and related concepts quantitatively influence their unique optical properties. In turn, they also provide guidance to evaluate rigorously how modifications in related families of molecules, including extended carbon chains, chemically functionalized molecules, and multiple metal-containing molecules, affect the spectroscopic features critical to optical cycling applications.

Materials and Methods

Metal acetylides were produced in a laser-ablation supersonic expansion source used by our group previously to study metal-bearing species (61, 101, 102), including most recently the closely related molecule magnesium dicarbide, MgC₂ (95). A dilute sample of acetylene (0.1%) in neon was pulsed into vacuum with a solenoid valve from a stagnation pressure of 2,500 torr in 400 to 600-µs pulses at a repetition rate of 5 Hz. After exiting the valve aperture, the gas passed a rotating metal target (Mg, Ca, or Sr), which was ablated with a focused (f = 50 cm) 50-mJ pulse of 532-nm radiation from the frequency-doubled output of an Nd:YAG laser (Surelite SLI-10), and a discharge region capped by two copper ring electrodes, which struck an 850 V DC discharge that increased the production efficiency in our source by up to a factor of five (103). The gas then expanded into vacuum along the axis of a large Fabry-Pérot microwave cavity formed by two spherical mirrors. A 1-µs pulse of resonant microwave radiation excited rotational transitions, and the subsequent free induction decay was digitally recorded and Fourier transformed. The cavity spectrometer operates over 5 to 26 GHz (104) and has a resonance line width of about

The gas pulse, laser ablation, and discharge conditions were initially tuned by optimizing the production of MgNC (105) (using CH₃CN instead of HCCH). We then searched for evidence of the metal acetylides near transition frequencies predicted by combining rotation and spin-rotation constants from mm-wave measurements of the main isotopologues (35–37) and our calculated hyperfine parameters and isotope shifts (see below). Ultimately, MgCCH, CaCCH, and SrCCH were each detected and produced with comparable abundance and source conditions. (We estimate 10^{10} to 10^{11} MCCH molecules per pulse, compared to 10^{15} HCCH precursor molecules and 10^{14} to 10^{15} ablated metal atoms per pulse.) The metal isotopes 24 Mg (79%), 25 Mg (10%), and 26 Mg (11%); 40 Ca (97%) and 44 Ca (2%); and 88 Sr (83%), 87 Sr (7%), and 86 Sr (10%) were observed in natural abundance (shown in parentheses). ²⁵Mg and ⁸⁷Sr both have nonzero nuclear spin, which is necessary to measure the electronic spin density at the metal atom. The only stable calcium isotope with a nonzero spin (⁴³Ca, 0.14%) is present at too low a concentration to detect in natural

abundance. Deuterated isotopologues were produced with a sample of DCCD, and both singly substituted ¹³C isotopologues with a statistical 1:1 sample of ¹²C/¹³C acetylene synthesized in our laboratory.

Theory. Ab initio calculations for the molecular properties of interest were performed with CFOUR (106, 107). Optimized geometries were obtained using all-electron (AE) coupled cluster calculations with singles, doubles, and perturbative triples [CCSD(T)] extrapolated across the Dunning correlationconsistent core-valence basis sets cc-pCVxZ with x = T, Q, and 5 (74, 76, 108– 113); for Ca and Sr the effective core potentials (ECP) ECP10MDF and ECP28MDF were used for the first 10 and 28 core electrons, respectively, along with the corresponding cc-pCVxZ-PP basis sets (114). For Mg, the 1s orbitals were omitted from the correlation treatment consistent with the original core-valence basis set optimization procedure (109). The effects of augmented basis sets on the geometry were estimated by optimization at the AE-CCSD(T)/aug-cc-pCVQZ level of theory, and high-order correlation corrections were estimated by performing geometry optimizations with frozen-core (FC)-CCSD(T) and FC-CCSDT(Q) using the cc-pVDZ basis set (and the cc-pVDZ-PP basis set along with the ECP for Ca and Sr). Second-order vibrational perturbation theory (VPT2) calculations were performed at the AE-CCSD(T)/cc-pCVTZ level of theory to obtain the zeropoint corrections for the rotational constants for each measured isotopologue $(B_e - B_0)$, the centrifugal distortion parameters and the vibrationally averaged dipole moments (115). The electronic spin-rotation coupling constants and electronic q-tensors were calculated at the FC-CCSD(T)/cc-pVQZ level of theory (116), the latter to correct for the electronic contribution to the semiexperimental equilibrium geometries. Finally, electric field gradients were calculated using the AE-CCSD(T)/cc-pCVQZ level of theory (115) to estimate the D and ²⁵Mg nuclear quadrupole coupling constants and AE-CCSD(T)/cc-pCVTZ for the ⁴³Ca coupling constant. The quadrupole coupling constant was not calculated for Sr, as electric field gradient evaluations are not implemented with ECPs in CFOUR.

Data, Materials, and Software Availability. All study data are included in the article and/or SI Appendix.

ACKNOWLEDGMENTS. This work is supported by the United States NSF (Award No. PHY-2110489) and the United States-Israel Binational Science Foundation (Grant No. 2020724). N.G.-D., E.B., T.G., and J.H.B. are also supported by the Israel Science Foundation (ISF), Grant No. 194/20. N.G.-D. acknowledges the VATAT scholarship for Ph.D. students in quantum science and technology. We are grateful to Profs. John F. Stanton (University of Florida) and Lan Cheng (Johns Hopkins University) for sharing their expertise with coupled cluster methods.

Author affiliations: ^aAtomic and Molecular Physics Division, Center for Astrophysics | Harvard & Smithsonian, Cambridge, MA 02138; and ^bDepartment of Chemistry, Ben-Gurion University of the Negev, Beer Sheva 8410501, Israel

Author contributions: P.B.C., N.G.-D., E.B., T.G., J.H.B., and M.C.M. designed research; performed research; analyzed data; and wrote the paper.

- M. S. Safronova et al., Search for new physics with atoms and molecules. Rev. Mod. Phys. 90, 025008 (2018).
- J. L. Bohn, A. M. Rey, J. Ye, Cold molecules: Progress in quantum engineering of chemistry and quantum matter. *Science* **357**, 1002–1010 (2017).
- J. F. Barry, E. S. Shuman, E. B. Norrgard, D. DeMille, Laser radiation pressure slowing of a molecular beam. Phys. Rev. Lett. 108, 103002 (2012).
- J. F. Barry, D. J. McCarron, E. B. Norrgard, M. H. Steinecker, D. DeMille, Magneto-optical trapping of a diatomic molecule. Nature 512, 286-289 (2014).
- E. S. Shuman, J. F. Barry, D. R. Glenn, D. DeMille, Radiative force from optical cycling on a diatomic molecule. Phys. Rev. Lett. 103, 223001 (2009).
- E. S. Shuman, J. F. Barry, D. DeMille, Laser cooling of a diatomic molecule. Nature 467, 820-823 (2010).
- L. Anderegg et al., Radio frequency magneto-optical trapping of CaF with high density. Phys. Rev. Lett. 119, 103201 (2017).
- L. Anderegg et al., Laser cooling of optically trapped molecules. Nat. Phys. 14, 890-893
- E. Chae et al., One-dimensional magneto-optical compression of a cold CaF molecular beam. New J. Phys. 19, 033035 (2017).
- B. Hemmerling et al., Laser slowing of CaF molecules to near the capture velocity of a molecular
- V. Zhelyazkova et al., Laser cooling and slowing of CaF molecules. Phys. Rev. A 89, 53416 (2014)
- MOT. J. Phys. B: At. Mol. Opt. Phys. 49, 174001 (2016).

- J. Lim et al., Laser cooled YbF molecules for measuring the electron's electric dipole moment. Phys. Rev Lett 120, 123201 (2018)
- M. T. Hummon et al., 2D magneto-optical trapping of diatomic molecules. Phys. Rev. Lett. 110, 143001 (2013)
- A. L. Collopy et al., 3D magneto-optical trap of yttrium monoxide. Phys. Rev. Lett. 121, 213201
- B. L. Augenbraun et al., Laser-cooled polyatomic molecules for improved electron electric dipole moment searches. New J. Phys. 22, 022003 (2020).
- I. Kozyryev, L. Baum, K. Matsuda, B. Hemmerling, J. M. Doyle, Radiation pressure force from optical cycling on a polyatomic molecule. J. Phys. B: At. Mol. Opt. Phys. 49, 134002 (2016).
- I. Kozyryev et al., Sisyphus laser cooling of a polyatomic molecule. Phys. Rev. Lett. 118, 173201
- N. B. Vilas et al., Magneto-optical trapping and sub-Doppler cooling of a polyatomic molecule. Nature 606, 70-74 (2022).
- D. Mitra et al., Direct laser cooling of a symmetric top molecule. Science 369, 1366-1369
- B. L. Augenbraun, S. Burchesky, A. Winnicki, J. M. Doyle, High-resolution laser spectroscopy of a functionalized aromatic molecule. J. Phys. Chem. Lett. 13, 10771–10777 (2022).
- B. L. Augenbraun et al., Observation and laser spectroscopy of ytterbium monomethoxide, YbOCH₃. Phys. Rev. A 103, 022814 (2021).
- M. J. O'Rourke, N. R. Hutzler, Hypermetallic polar molecules for precision measurements. Phys. Rev. A 100, 022502 (2019).

- M. V. Ivanov, S. Gulania, A. I. Krylov, Two cycling centers in one molecule: Communication by through-bond interactions and entanglement of the unpaired electrons. J. Phys. Chem. Lett. 11,
- J. Klos, S. Kotochigova, Prospects for laser cooling of polyatomic molecules with increasing complexity. Phys. Rev. Res. 2, 13384 (2020).
- G. Z. Zhu et al., Functionalizing aromatic compounds with optical cycling centres. Nat. Chem. 14,
- C. E. Dickerson et al., Franck-Condon tuning of optical cycling centers by organic 26. functionalization. Phys. Rev. Lett. 126, 123002 (2021).
- D. Mitra et al., Pathway toward optical cycling and laser cooling of functionalized Arenes. J. Phys. Chem. Lett. 13, 7029-7035 (2022).
- A. M. Ellis, Main group metal-ligand interactions in small molecules: New insights from laser 28. spectroscopy. Int. Rev. Phys. Chem. 20, 551–590 (2001).
- L. Baum et al., Establishing a nearly closed cycling transition in a polyatomic molecule. Phys. Rev. 29 A 103, 043111 (2021).
- C. Zhang *et al.*, Accurate prediction and measurement of vibronic branching ratios for laser cooling linear polyatomic molecules. *J. Chem. Phys.* **155**, 091101 (2021).

 Z. Lasner, A. Lunstad, C. Zhang, L. Cheng, J. M. Doyle, Vibronic branching ratios for nearly closed 30.
- 31. rapid photon cycling of SrOH. Phys. Rev. A 106, L020801 (2022).
- E. T. Mengesha et al., Branching ratios, radiative lifetimes, and transition dipole moments for 32. YbOH. J. Phys. Chem. A 124, 3135-3148 (2020).
- M. V. Ivanov, F. H. Bangerter, P. Wójcik, A. I. Krylov, Toward ultracold organic chemistry: Prospects of laser cooling large organic molecules. J. Phys. Chem. Lett. 11, 6670-6676 (2020).
- M. A. Anderson, L. M. Ziurys, Laboratory detection and millimeter spectrum of the MgCCH radical. Astrophys. J. 439, L25 (1995).
- M. Brewster, A. Apponi, J. Xin, L. Ziurys, Millimeter-wave spectroscopy of vibrationally-excited 35. NaCCH ($\tilde{X}^1\Sigma^+$) and MgCCH ($\tilde{X}^2\Sigma^+$): The ν_5 bending mode. Chem. Phys. Lett. **310**, 411–422 (1999).
- M. A. Anderson, L. M. Ziurys, The millimeter/submillimeter rotational spectrum of CaCCH($X^2 \Sigma^+$). Astrophys. J. **444**, L57 (1995).
- B. P. Nuccio, A. J. Apponi, L. M. Ziurys, The millimeter-wave spectrum of SrCCH(X $^2\Sigma^+$): Chemical trends in metal monoacetylide species. Chem. Phys. Lett. 247, 283-288 (1995).
- G. K. Corlett, A. M. Little, A. M. Ellis, LIF spectroscopy of the MgCCH free radical. Chem. Phys. Lett. **249**, 53-58 (1996).
- G. K. Corlett, M. S. Beardah, A. M. Ellis, A dispersed fluorescence investigation of the low
- frequency vibrations of MgCCH(\tilde{X}^2 Σ^+). *J. Mol. Spectrosc.* **185**, 202–203 (1997). A. M. R. P. Bopegedera, C. R. Brazier, P. F. Bernath, Laser spectroscopy of calcium and strontium monoacetylides. Chem. Phys. Lett. 136, 97-100 (1987).
- A. M. Bopegedera, C. R. Brazier, P. F. Bernath, Rotational analysis of the $\tilde{A}^2\Pi \tilde{\chi}^2\Sigma^+$ transition of calcium monoacetylide, CaCCH. J. Mol. Spectrosc. 129, 268-275 (1988).
- C. J. Whitham, B. Soep, J. P. Visticot, A. Keller, Observation and spectroscopy of metallic free radicals produced by reactive collisions during a supersonic expansion. J. Chem. Phys. 93, 991 (1990).
- A. J. Marr, J. Perry, T. C. Steimle, A molecular beam optical/Stark study of calcium monoacetylide. J. Chem. Phys. **103**, 3861–3863 (1995). 43.
- M. Li, J. A. Coxon, Laser spectroscopy of the $\tilde{A}^2\Pi \tilde{\chi}^2\Sigma^+$ 0-0 band of the CaCCH radical. J. Mol. Spectrosc. 176, 206-210 (1996).
- M. Li, J. A. Coxon, The first excited Ca-C-C bending vibration levels in the $\tilde{A}^2\Pi$ and $\tilde{X}^2\Sigma^+$ states of the CaCCH radical: The Renner-Teller effect and K-type resonance. J. Mol. Spectrosc. 180, 287-297 (1996).
- M. Li, J. A. Coxon, The ν_3 and $\nu_3 + \nu_5$ vibration levels in the CaCCH $\tilde{\chi}^2 \Sigma^+$ state. *J. Mol.* Spectrosc. 184, 395-400 (1997).
- M. Li, J. A. Coxon, The CaCCH $\tilde{A}^2\Pi$ · $\tilde{X}^2\Sigma^+$ 5 2_2 and 5 2_2 bands studied by high resolution spectroscopy: The Ca-C-C bending vibration and vibronic interaction. J. Mol. Spectrosc. 183, 250-262 (1997).
- M. Li, J. A. Coxon, The C-C-H bending vibration mode (ν 4) in the electronic $\tilde{A}^2\Pi$ and $\tilde{A}^2\Sigma^+$ states of the CaCCH radical. *J. Mol. Spectrosc.* **196**, 14–19 (1999).
- G. M. Greetham, A. M. Ellis, Laser-induced fluorescence spectrum of the orbitally forbidden $\tilde{B}^{\prime 2}\Delta - \tilde{X}^2\Sigma^+$ transition of SrCCH. J. Mol. Spectrosc. **206**, 198–199 (2001).
- M. J. Dick, P. M. Sheridan, J. G. Wang, P. F. Bernath, A high-resolution laser ablation study of the $\tilde{A}^2\Pi- ilde{X}^2\Sigma^+$ transition of SrCCH. *J. Mol. Spectrosc.* **233**, 197–202 (2005).
- D. W. Tokaryk, A. G. Adam, W. S. Hopkins, High-resolution laser spectroscopy of the $\tilde{A}^2\Pi$ $\tilde{\chi}^2 \Sigma^+$ transition of MgCCH. J. Mol. Spectrosc. **230**, 54–61 (2005).
- D. Tokaryk, A. Adam, M. Slaney, Cavity ring down laser spectroscopy of the $\tilde{B}^2\Sigma^+ \tilde{X}^2\Sigma^+$ transition of CaCCH. *Chem. Phys. Lett.* **433**, 264–267 (2007).
- A. Faridian, D. Tokaryk, A. Adam, Laser spectroscopy of the $\tilde{A}^2\Pi \tilde{X}^2\Sigma^+$ and $\tilde{B}^2\Sigma^+ \tilde{X}^2\Sigma^+$ transitions of CaCCD. J. Mol. Spectrosc. 264, 125-128 (2010).
- A. Faridian, D. Tokaryk, A. Adam, Laser spectroscopy of the $\tilde{A}^2\Pi-\tilde{X}^2\Sigma^+$ transitions of SrCCH and SrCCD. *J. Mol. Spectrosc.* **266**, 116–118 (2011).
- R. A. Frosch, H. M. Foley, Magnetic hyperfine structure in diatomic molecules. Phys. Rev. 88, 55. 1337 (1952).
- C. H. Townes, A. L. Schawlow, Microwave Spectroscopy (Dover, New York, NY, 1975).
- 57. H. M. Pickett, The fitting and prediction of vibration-rotation spectra with spin interactions. J. Mol. Spectrosc. 148, 371-377 (1991).
- W. H. Flygare, Magnetic interactions in molecules and an analysis of molecular electronic charge distribution from magnetic parameters. Chem. Rev. 74, 653-687 (1974).
- D. E. Woon, Ab Initio characterization of MgCCH, MgCCH+, and MgC₂ and pathways to their formation in the interstellar medium. Astrophys. J. 456, 602 (1996).
- M. Wang et al., The AME2016 atomic mass evaluation (II). Tables, graphs and references. Chin. Phys. C 41, 030003 (2017).
- S. Brünken, H. S. P. Müller, K. M. Menten, M. C. McCarthy, P. Thaddeus, The rotational spectrum of TiO₂. Astrophys. J. **676**, 1367–1371 (2008).
- X. Huang, T. J. Lee, Accurate ab initio quartic force fields for NH₂ and CCH⁻ and rovibrational spectroscopic constants for their isotopologs. J. Chem. Phys. 131, 104301 (2009).

- M. Mladenović, P. Botschwina, P. Sebald, S. Carter, A theoretical study of the acetylide anion, HCC-. Theor. Chem. Acc. 100, 134-146 (1998).
- F. Tamassia, E. Cané, L. Fusina, G. Di Lonardo, The experimental equilibrium structure of acetylene. *Phys. Chem. Chem. Phys.* **18**, 1937–1944 (2016). P. G. Szalay, L. S. Thøgersen, J. Olsen, M. Kállay, J. Gauss, Equilibrium geometry of the ethynyl
- (CCH) radical. J. Phys. Chem. A 108, 3030-3034 (2004).
- C. A. Gottlieb, E. W. Gottlieb, P. Thaddeus, Laboratory and astronomical measurement of the millimeter wave spectrum of the ethynyl radical CCH. Astrophys. J. 264, 740-745 (1983).
- M. C. McCarthy, C. A. Gottlieb, P. Thaddeus, Rotational spectrum and hyperfine structure of 67. ¹³CCH and C¹³CH. J. Mol. Spectrosc. **173**, 303–307 (1995).
- M. A. Anderson, M. D. Allen, L. M. Ziurys, Millimeter-wave spectroscopy of MgF: Structure and 68.
- M. A. Anderson, M. D. Anien, L. M. Zurys, Millmeter-wave spectroscopy of MgF: Structure and bonding in alkaline-earth monofluoride radicals. *J. Chem. Phys.* **100**, 824 (1994). J. Nakagawa, P. J. Domaille, T. C. Steimle, D. O. Harris, Microwave optical double resonance and reanalysis of the CaF $A^2\Pi_T X^2\Sigma$ band system. *J. Mol. Spectrosc.* **70**, 374–385 (1978). H. U. Schütze-Pahlmann, C. Ryzlewicz, J. Hoeft, T. Törring, Millimeter wave spectra of the $^2\Sigma$ radicals SrF and SrCl. *Chem. Phys. Lett.* **93**, 74–77 (1982). 69.
- 70.
- A. J. Apponi, M. A. Anderson, L. M. Ziurys, High resolution spectroscopy of MgOH ($\chi^2 \Sigma^+$) in its V₂ mode: Further evidence for quasilinearity. *J. Chem. Phys.* **111**, 10919–10925 (1999).
- M. Li, J. A. Coxon, High-resolution analysis of the fundamental bending vibrations in the $\tilde{A}^2 \Pi$ and $\tilde{\chi}^2\Sigma^+$ states of CaOH and CaOD: Deperturbation of Renner-Teller, spin-orbit and K-type resonance interactions. J. Chem. Phys. 102, 2663-2674 (1995).
- M. A. Anderson, W. L. Barclay, L. M. Ziurys, The millimeter-wave spectrum of the SrOH and SrOD radicals. Chem. Phys. Lett. 196, 166-172 (1992).
- J. H. Baraban et al., The molecular structure of gauche-1,3-butadiene: Experimental establishment of non-planarity. Angew. Chem. 130, 1839-1843 (2018).
- J. H. Baraban, D. A. Matthews, J. F. Stanton, Communication: An accurate calculation of the S1 C2H2 cis-trans isomerization barrier height. J. Chem. Phys. 144, 111102 (2016).
- J. H. Baraban, P. B. Changala, J. F. Stanton, The equilibrium structure of hydrogen peroxide. J. Mol. Spectrosc. 343, 92-95 (2018).
- N. Genossar, J. P. Porterfield, J. H. Baraban, Decomposition of the simplest ketohydroperoxide in the ozonolysis of ethylene. *Phys. Chem. Chem. Phys.* **22**, 16949–16955 (2020).

 Z. T. Xu *et al.*, Precision measurement of the ²⁵Mg⁺ ground-state hyperfine constant. *Phys. Rev.*
- A 96, 052507 (2017).
- S. M. Brewer $\dot{\it et\,al.}$, Measurements of $^{27}{\rm Al}^+$ and $^{25}{\rm Mg}^+$ magnetic constants for improved ion-clock accuracy. *Phys. Rev. A* **100**, 013409 (2019).
- H. Sunaoshi $\it et\,al.$, A precision measurement of the hyperfine structure of $^{87}{\rm Sr}^+$. Hyperfine Interact. 78, 241-245 (1993).
- D. T. Yordanov et al., Quadrupole moments of ²⁹ Mg and ³³ Mg. Hyperfine Interact. **240**, 67 81. (2019).
- C. Sur, B. K. Sahoo, R. K. Chaudhuri, B. P. Das, D. Mukherjee, Comparative studies of the magnetic dipole and electric quadrupole hyperfine constants for the ground and low lying excited states of ²⁵Mg⁺. Eur. Phys. J. D **32**, 25-31 (2005).
- F. Buchinger et al., Systematics of nuclear ground state properties in ^{78–100} Sr by laser spectroscopy. Phys. Rev. C 41, 2883 (1990).
- spectroscopy. *Trys. nev.* C **41**, 2003 (1770). A. Lurio, Hyperfine structure of the ³ P states of Zn⁶⁷ and Mg²⁵. *Phys. Rev.* **126**, 1768 (1962). S. M. Heider, G. O. Brink, Hyperfine structure of ⁸⁷ Sr in the ³ P₂ metastable state. *Phys. Rev.* A **16**,
- 1371-1374 (1977)
- F. DeLucia, W. Gordy, Molecular-beam maser for the shorter-millimeter-wave region: Spectral 86 constants of HCN and DCN. Phys. Rev. 187, 58-65 (1969).
- S. C. Wofsy, J. S. Muenter, W. Klemperer, Hyperfine structure and dipole moment of CH₃D. 3. C. worsy, 3. S. Mueriter, M. Kemperer, hypermie structure and dipole moment of Cr₃D.

 J. Chem. Phys. **53**, 4005–4014 (1970).

 R. L. Deleon, J. S. Muenter, Radiofrequency spectroscopy of DCCD: Deuterium quadrupole coupling in acetylene. *J. Mol. Spectrosc.* **126**, 13–18 (1987).

 H. Coker, Empirical free-ion polarizabilities of the alkali metal, alkaline earth metal, and halide
- 88
- 89 ions. J. Phys. Chem. 80, 2078-2084 (1976).
- P. Sheridan et al., Fourier transform microwave spectroscopy of LiCCH, NaCCH, and KCCH: Quadrupole hyperfine interactions in alkali monoacetylides. J. Mol. Spectrosc. 269, 231–235
- R. R. Freeman, D. Kleppner, Core polarization and quantum defects in high-angular-momentum states of alkali atoms. Phys. Rev. A 14, 1614-1619 (1976).
- A. Kramida, Yu. Ralchenko, J. Reader, NIST ASD Team, NIST Atomic Spectra Database (ver. 5.10 (National Institute of Standards and Technology, Gaithersburg, MD, 2022). https://physics.nist. gov/asd. Accessed 14 February 2023.
- P. Schwerdtfeger, J. K. Nagle, 2018 Table of static dipole polarizabilities of the neutral elements in the periodic table. Mol. Phys. 117, 1200-1225 (2019).
- W. Xia, H. Ma, W. Bian, Production of ultracold CaCCH and SrCCH molecules by direct laser cooling: A theoretical study based on accurate ab initio calculations. J. Chem. Phys. 155, 204304 (2021).
- P. B. Changala et al., Laboratory and astronomical discovery of magnesium dicarbide, MgC₂. Astrophys. J. Lett. **940**, L42 (2022).
- M. Bixon, J. Jortner, Intramolecular radiationless transitions. J. Chem. Phys. 48, 715-726 (1968). 96
- N. H. Pilgram, A. Jadbabaie, Y. Zeng, N. R. Hutzler, T. C. Steimle, Fine and hyperfine interactions in 171 YbOH and 173 YbOH. *J. Chem. Phys.* **154**, 244309 (2021). 97.
- F. Kogel, M. Rockenhäuser, R. Albrecht, T. Langen, A laser cooling scheme for precision measurements using fermionic barium monofluoride (137 Ba19 F) molecules. *New J. Phys.* 23, 095003 (2021).
- V. V. Albert, J. P. Covey, J. Preskill, Robust encoding of a qubit in a molecule. Phys. Rev. X 10, 031050 (2020).
- R. J. McMahon et al., The radio spectrum of the phenyl radical. Astrophys. J. Lett. 590, L61-L64
- O. Zingsheim et al., Germanium dicarbide: Evidence for a T-shaped ground state structure. J. Phys. Chem. Lett. 8, 3776-3781 (2017).
- K. L. K. Lee, S. Thorwirth, M. A. Martin-Drumel, M. C. McCarthy, Generation and structural characterization of Ge carbides GeC_n (n = 4, 5, 6) by laser ablation, broadband rotational spectroscopy, and quantum chemistry. Phys. Chem. Chem. Phys. 21, 18911-18919

- 103. M. Sun *et al.*, The rotational spectrum of CuCCH($\tilde{\chi}^1\Sigma^+$): A Fourier transform microwave discharge assisted laser ablation spectroscopy and millimeter/submillimeter study. J. Chem. Phys. 133, 174301 (2010).
- K. N. Crabtree et al., Microwave spectral taxonomy: A semi-automated combination of chirped-
- pulse and cavity Fourier-transform microwave spectroscopy. *J. Chem. Phys.* **144**, 124201 (2016). K. A. Walker, M. C. Gerry, 14 N hyperfine structure in the pure rotational spectrum of 24 Mg 14 N 12 C. J. Mol. Spectrosc. 189, 40-45 (1998).
- J. Mol. Spectrosc. 189, 40-45 (1998).
 J. F. Stanton et al., CFOUR, Coupled-Cluster techniques for Computational Chemistry, a quantum-chemical program package. (year?) With contributions from A.A. Auer, R.J. Bartlett, U. Benedikt, C. Berger, D.E. Bernholdt, Y.J. Bomble, O. Christiansen, F. Engel, R. Faber, M. Heckert, O. Heun, M. Hilgenberg, C. Huber, T.-C. Jagau, D. Jonsson, J. Jusélius, T. Kirsch, K. Klein, W.J. Lauderdale, F. Lipparini, T. Metzroth, L.A. Mück, D.P. O'Neill, D.R. Price, E. Prochnow, C. Puzzarini, K. Ruud, F. Schiffmann, W. Schwalbach, C. Simmons, S. Stopkowicz, A. Tajti, J. Vázquez, F. Wang, J.D. Watts and the integral packages MOLECULE (J. Almlöf and P.R. Taylor), PROPS (P.R. Taylor), ABACUS (T. Helpaker, H.J. Aa. Jensen, P. Jørgensen, and J. Olsen), and FCP routines by A. V. ABACUS (T. Helgaker, H.J. Aa. Jensen, P. Jørgensen, and J. Olsen), and ECP routines by A. V. Mitin and C. van Wüllen. For the current version, see http://www.cfour.de. Accessed 1 March 2022
- 107 D. A. Matthews et al., Coupled-cluster techniques for computational chemistry: The CFOUR program package. J. Chem. Phys. 152, 214108 (2020).
- T. H. Dunning Jr, Gaussian basis sets for use in correlated molecular calculations. I. The atoms boron through neon and hydrogen. *J. Chem. Phys.* **90**, 1007–1023 (1989).

- 109. B. P. Prascher, D. E. Woon, K. A. Peterson, T. H. Dunning, A. K. Wilson, Gaussian basis sets for use in correlated molecular calculations. VII. Valence, core-valence, and scalar relativistic basis sets for Li, Be, Na, and Mg. Theor. Chem. Acc. 128, 69-82 (2011).
- 110. J. G. Hill, K. A. Peterson, Gaussian basis sets for use in correlated molecular calculations. XI. Pseudopotential-based and all-electron relativistic basis sets for alkali metal (K-Fr) and alkaline earth (Ca-Ra) elements. J. Chem. Phys. 147, 244106 (2017).
- J. Gauss, D. Cremer, J. F. Stanton, The re structure of cyclopropane. J. Phys. Chem. A 104, 1319-1324 (2000).
- C. Puzzarini, Extrapolation to the complete basis set limit of structural parameters: Comparison of different approaches. *J. Phys. Chem. A* **113**, 14530–14535 (2009).
- M. A. Martin-Drumel, J. H. Baraban, P. B. Changala, J. F. Stanton, M. C. McCarthy, The hunt for elusive molecules: Insights from joint theoretical and experimental investigations. *Chem. Eur. J.* **25**, 7243-7258 (2019).
- 114. I. S. Lim, H. Stoll, P. Schwerdtfeger, Relativistic small-core energy-consistent pseudopotentials for the alkaline-earth elements from Ca to Ra. J. Chem. Phys. 124, 034107 (2006).
- C. Puzzarini, J. F. Stanton, J. Gauss, Quantum-chemical calculation of spectroscopic parameters for rotational spectroscopy. *Int. Rev. Phys. Chem.* **29**, 273–367 (2010).

 J. Gauss, M. Kallay, F. Neese, Calculation of electronic g-Tensors using coupled cluster theory.
- J. Phys. Chem. A 113, 11541-11549 (2009).